Metascience in Aerospace

Research article

Numerical simulation of vortex-induced vibration in a bladeless turbine: Effects of separation distance between tandem harvesters

Dulce M Graciano[1], Fernando Z Sierra-Espinosa[2,*] and Juan C García[2]

[1] Posgrado en Ingeniería y Ciencias Aplicadas, Autonomous University of Morelos State, 101 Av. Universidad, Chamilpa, Mor. 62209, Mexico

[2] Centro de Investigación en Ingeniería y Ciencias Aplicadas, Autonomous University of Morelos State, 101 Av. Universidad, Chamilpa, Mor. 62209, Mexico

* **Correspondence:** Email: fse@uaem.mx.

Abstract: Bladeless wind turbines are attracting attention as energy harvesters due to several conveniences like the ease of construction and suitability for operating under small wind speed. As a grouped energy generation system, it is likely the simplest configuration compared to wind farms. However, the characterization of tandem harvesters requires a deep understanding of the effects produced by the interaction of the two. Therefore, this work considered a set of two conical cylinders representing tandem harvesters, which lie on the bottom of a wind tunnel and were subjected to resonance conditions. The attention focused on evaluating the effects of separation distance between conical cylinders by three distances: $\ell = 0.25h$, $0.5h$, and $0.75h$, where h is the cylinder's total height. Oscillation due to vortex shedding was numerically predicted. The analysis centered on the fluid-structure interaction in pairs of wind generators subjected to wind-induced resonance, and how the distance between them affects their oscillation. Experimental data of cylinder vibration measured in a wind tunnel served to validate the numerical results. The results showed strong effects of the wake on the second cylinder placed downstream from the first one for a distance $\ell = 0.25h$. In contrast, minimum effects were observed for $\ell = 0.5h$ and $\ell = 0.75h$.

1. Introduction

Several technologies are being developed to convert kinetic wind energy into electrical energy. Traditionally, this conversion is performed by horizontal-axis wind turbines, which must be installed at significant distances from each other to avoid wind flow disturbances. An emerging technology that promises to overcome this limitation is the bladeless turbine. These devices operate on the principle of vortex-induced vibrations (VIV), a phenomenon that occurs due to the interaction between the fluid (air) and the structure. When the body responds freely, either due to being mounted elastically or its own flexibility, it can oscillate in two directions, in the stream-wise direction and perpendicularly, or a combination of both, resulting in VIV [1]. VIV is a phenomenon that occurs due to the detachment of the boundary layer around the body, whose behavior depends on the shape of the body, the flow conditions, and the orientation with respect to the flow direction. The boundary layer is a region where viscous effects are not negligible, and thus large velocity gradients are present. Studies by [2–13] have examined the behavior of this flow region and report a decrease of thickness as the Reynolds number increases. However, under separation conditions, the boundary layer separates and forms vortices behind the body, alternately from one side of the body to another giving rise to the vortex wake, known as a vortex street. The frequency of vortex shedding depends on the flow velocity and the geometry characteristics of the body. An interpretation is that the mutual interaction between two free shear layers is a key factor in the formation of vortex streets and postulates three conditions for fluid particles in the opposite shear layer that traverse the wake [14]: a) they can be entrained into the growing vortex, thereby reducing its strength, b) they can find their way into the shear layer with a vorticity of the opposite sign to theirs, and c) they can feedback into the near-wake region. The amount of fluid following these routes controls the shedding frequency, the strength of the shed vortices, and the base pressure.

Alternating vortex shedding has been characterized by authors [15–24] through the Reynolds and Strouhal numbers', *Re-St*, relationship, with the circular cross-section cylinder being the most studied body shape. The results are presented as correlation equations as a function of the *Re* number. For $0 < Re < 200$ and $200 < Re < 400$, Equations (1) and (2) apply, respectively [21]. For $Re > 1000$, Equation (3) is suggested [22], while for a range of $300 < Re < 2000$, Equation (4) is suggested [23]. Generally, Equation (5) is used for $47 < Re < 2 \times 10^5$, where St^* and m are coefficients that vary with *Re* [24]. Additionally, this relationship is subjected to the geometry of the body [25].

$$St = 0.2175 - \frac{5.10647}{Re} \tag{1}$$

$$St = 0.2120 - \frac{2.7}{Re} \tag{2}$$

$$St = 0.2698 - \frac{1.0271}{\sqrt{Re}} \tag{3}$$

$$St = 0.2120(1 - \frac{12.7}{Re}) \tag{4}$$

$$St = St^* + \frac{m}{\sqrt{Re}} \tag{5}$$

On the other hand, the amplitude of body motion due to vortex-induced vibrations depends on the vortex shedding frequency, with a maximum for a synchrony between this frequency and the natural frequency of the body. As mentioned earlier, the vortex shedding frequency is a function of the *Re* number, so the range of synchronization also depends on *Re*. The literature survey revealed four kinds of synchronization for cylinder fluid as follows [26–27]:

1. **Initial Excitation**: The vortex shedding frequency is smaller than the natural frequency of the body, resulting in oscillation amplitudes around 0.4 diameter.

2. **Synchronization**: The vortex shedding frequency is near the natural frequency, with oscillation amplitudes up to 2 diameter.

3. **Low Synchronization**: The vortex shedding frequency is larger than the natural frequency, resulting in amplitudes around 0.6 diameter.

4. **Desynchronization**: The vortex shedding frequency is too different compared to the natural frequency of the body, resulting in small amplitudes, around 0.1 diameter.

Bladeless turbines like the ones studied in this work are semi-rigid structures in the stage of commercialization [28]. These turbines aim to operate in synchrony under resonance conditions. The key characteristics of bladeless wind turbines, such as shape, roughness, and reduced mass, play a significant role in determining the VIV phenomenon and influencing their operational performance. According to Chizfahm [29], the shape of the turbine significantly affects its performance. Conical-shaped blade turbines perform more efficiently at higher wind speeds, while circular-shaped ones are optimized for lower wind speeds. This indicates that shape tuning can expand their operational wind range. Additionally, González [30] highlights that an increase in the diameter of the turbine correlates with higher *rms* values, indicating improved energy generation capacity. Surface roughness slightly reduces the lock-in range of the turbine, potentially affecting the overall performance, particularly for slender circular designs. Experimental results indicate that to optimize the energy utilization from a flowing fluid in a confined space, a set of bladeless turbines is suggested [31]. However, the effects of two structures interacting with the same flow in a limited space are defined by the distance between them. This is because this distance has influence on the vortex wake and, consequently, it plays a role on the oscillation displacements of the structures. Moreover, the fluid direction and the shape of the turbine combine with the spacing to define the behavior of the tandem bodies. It is observed that the streamlines behave differently compared with those around an isolated body [32–36]. Developers expect these turbines to perform well together while interacting, provided they are placed at a certain distance from each other, estimated as a half the total height of the body [28]. Although, when two tandem bodies oscillate, their oscillation amplitude defines their mutual interaction [37–38], such that a "wake stiffness" occurs from the vortex wake of the upstream tandem body equal to a linear spring for the oscillation of the downstream body [39]. For instance, a separation ratio between bodies (length/diameter) larger than 3.0 ensures the downstream body influences little on the oscillations of the upstream body [40–41]. However, for bodies of variable diameter, the effects can vary. Therefore, this work examines the behavior of the vortex wake in two tandem cylinders with different separation ratios and *Re* numbers using two-dimensional computational fluid dynamics (CFD) models and experimental flow fields. The paper shows that a downstream cylinder is subjected to high levels of turbulence generated by the upstream cylinder in agreement with other reports [30,42]. It was found that the shape of the vortex wake behind the upstream cylinder is directly linked to the phase angle of the cylinder oscillation and the Reynolds number.

The angle of attack significantly influences the VIV behavior for tandem bodies. It is defined as the angle between the flow direction and the central line connecting the bodies. Notably, the main VIV responses occur for 0° and 90° angles of attack, while responses for other angles are almost neglected

[43]. This study specifically focuses on the case of a 0° angle of attack. Although it is known that the angle of attack is important for tandem bodies, which is the angle between the flow direction and the central line between them, this work limits to the case of no angle of attack. Furthermore, since a distance between bodies larger than 2.7D makes the upstream body isolated [37] and, besides, the oscillation amplitude of two cylinders in a tandem arrangement reaches a minimum value when the spacing distance is 3.5D [42–44], this study is limited to distances equal to or smaller than 0.75h. In terms of energy harnessed, recent results indicate that a lighter mass and a larger diameter body can be more efficient for generating electricity [45]. Also, reducing the mass or increasing the stiffness or characteristic length of a vortex-induced generator allows a broader synchronization range, in favor of the output power and the range of fluid velocity [46]. While excessive damping reduces the oscillation amplitude and may even suppress vortex-induced vibrations, it helps to synchronize their oscillation movement more easily because the lower oscillation amplitudes cause a higher coupling level in VIV [47–49].

The studies mentioned above indicate that a systematic investigation on the distance between tandem bladeless turbines is lacking. Furthermore, how this distance affects each one in tandem configurations of bladeless generators is not known. Therefore, the present work investigates these two aspects of tandem bladeless generators. The following sections describe how this numerical research focused on this topic, which was validated with experimental data. Some guides for future directions will be given at the end, in the Conclusions section.
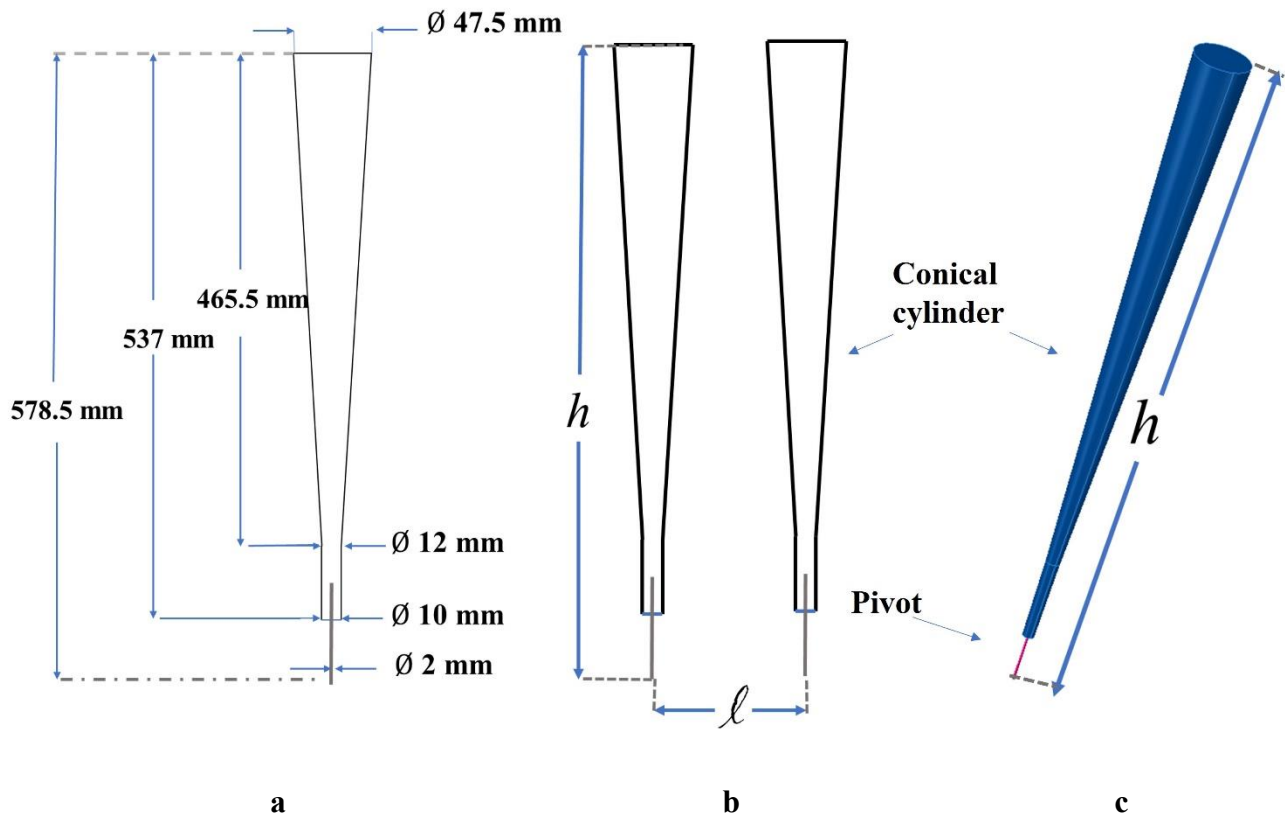
2.   Methods and data sources

This section describes the characteristics of the bladeless turbine and the wind tunnel, starting with details of geometry, materials, and dimensions. In principle, the geometry aspects of the physical model are in agreement with the computational modeling, making a direct comparison of results possible, from numerical simulation to experimental data. The computational model reproduces the experimental prototype except for the size, since the prototype was made at a 1:2 scale of the numerical model.

Two different materials constitute the bladeless generator model: the first one is a flexible pivot that supports the conical cylinder and is allocated inside the main body. The pivot allows 2 degrees of freedom to the system since it is of flexible carbon fiber material. Instead, the main body, a 3-D printed conical cylinder, is made of polylactic acid of variable diameter.

2.1. Geometry and aspect ratio

The bladeless turbine under study is a model shown in Figure 1a–d scaled 1:1 from one reported by Cajas et al. [50]. Figures 1a–c show the model, composed of the pivot and the conical cylinder. The main dimensions are shown together with a list of materials and properties, which defined the boundary conditions, discussed below. The flexibility of the pivot allowed the conical cylinder the 2D of freedom to oscillate under the strength of the airflow. The domain is a group of two models separated by distance ℓ as shown in Figure 1b. An isometric view is shown in Figure 1c for a more detailed description.

Figure 1. Main characteristics of the bladeless model, with details of construction: a) Single bladeless turbine with the detail of constitution fixed to the bottom of the wind tunnel, not to scale; b) Group of two bladeless turbines separated by a distance given as a function of the height, not to scale; c) Isometric 3D view of the conical cylinder; d) Details of bladeless structure.

The distance ℓ varied as a function of the height h as: $\ell = 0.25h$, $0.5h$, and $0.75h$.

The value of h is given in Figure 1. An aspect ratio, H, that represents the slenderness for which the results are valid, is defined as:

$$H = \frac{D}{h} \qquad (6)$$

where D represents a diameter relation as:

$$D = \frac{d_{min} + d_{max}}{2} \qquad (7)$$

with the minimum diameter: $dmin = 10\ mm,$ and a maximum diameter: $dmax = 47.5\ mm$, as shown in Figure 1a. On the other hand, the reduced mass m^* was taken into account by the following expression:
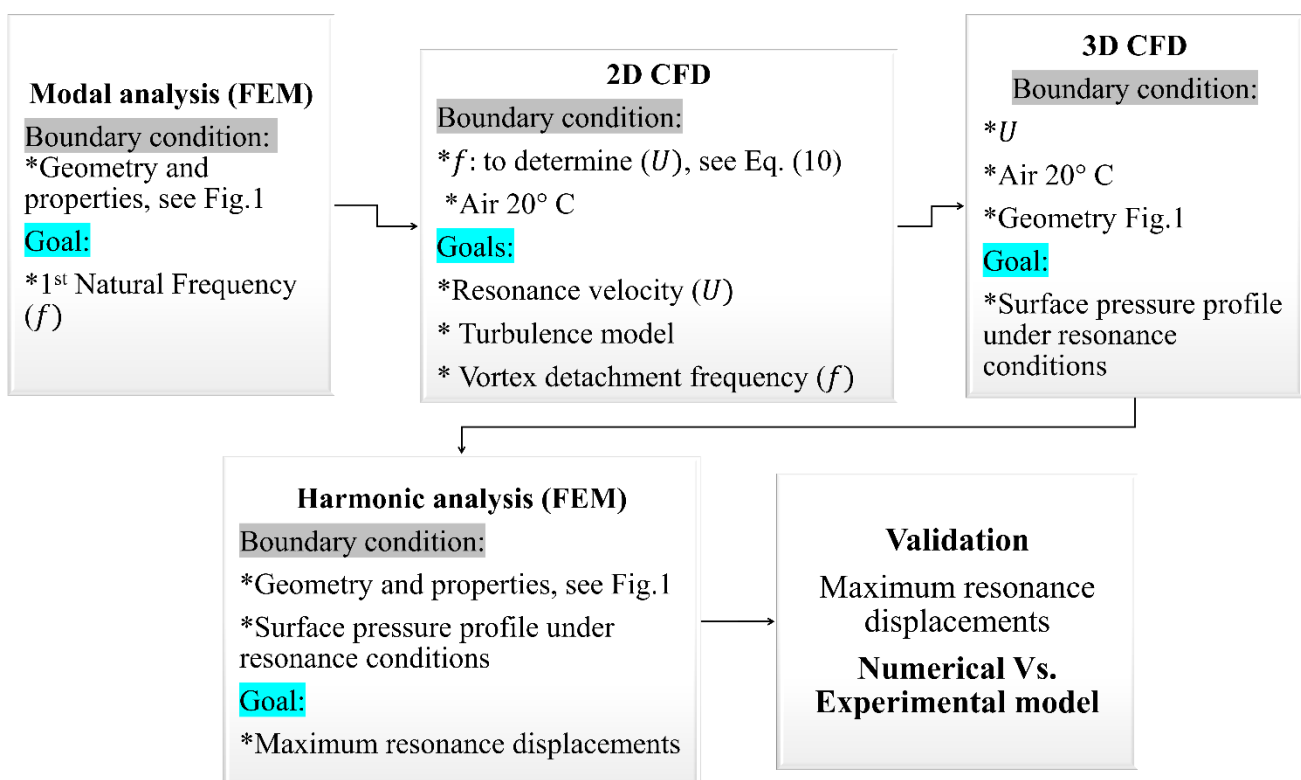
$$m^* = \frac{m_s}{\rho h D^2} \tag{8}$$

where ρ is the fluid density, and m_s is defined as:

$$m_s = \rho_m A \tag{9}$$

with ρ_m representing the density of the body structure, and A representing the transversal cross-area of the pivot.

2.2. Computational modeling

Modal analysis (FEM)
Boundary condition:
*Geometry and properties, see Fig.1
Goal:
*1st Natural Frequency (f)

2D CFD
Boundary condition:
*f: to determine (U), see Eq. (10)
*Air 20° C
Goals:
*Resonance velocity (U)
* Turbulence model
* Vortex detachment frequency (f)

3D CFD
Boundary condition:
*U
*Air 20° C
*Geometry Fig.1
Goal:
*Surface pressure profile under resonance conditions

Harmonic analysis (FEM)
Boundary condition:
*Geometry and properties, see Fig.1
*Surface pressure profile under resonance conditions
Goal:
*Maximum resonance displacements

Validation
Maximum resonance displacements
**Numerical Vs. Experimental model**

Figure 2. Flowchart of the modeling procedure combining the CFD and FEM approaches.

The methodology adopted in the computational modeling combines the approaches of finite element modeling (FEM) and computational fluid dynamics (CFD). This combination is needed in order to define the boundary conditions in every stage of the subsequent calculations until reaching the goal. Simultaneous solutions for fluid phase equations and structural equations have been reported for solving the VIV problem in ocean risers [51]. However, for the present work, decoupled solutions were adopted. Figure 2 shows a flowchart of the modeling, which was adopted in this work to simulate the body displacement on the second tandem bladeless generator as a consequence of vortex shedding from the first tandem bladeless generator. This effect is simulated for three separation distances from each other. The sequence of computational modeling starts with a modal analysis using FEM to identify the resonance condition of the turbine. Subsequently, 2D CFD simulations were performed on an

isolated bladeless turbine to determine the resonance velocity and select the turbulence model that best reproduced the vortex shedding phenomenon. Once these key parameters were identified, 2D CFD simulations again were carried out on two bladeless turbines arranged in tandem to assess the impact of different separation distances on vortex shedding. Afterward, 3D CFD simulations were conducted for both an isolated turbine and turbines in tandem, using the previously determined resonance velocity. Finally, a harmonic analysis was performed, with the resonance frequency and the pressure profiles obtained from the 3D CFD simulations, used as boundary conditions. The displacement results for the isolated turbine were compared with experimental wind tunnel data from a 1:2 scale model in interaction with an incompressible airstream fluid flow as described ahead.

A 3-D computational tetrahedral and non-structured mesh was built to define the domain that represents the interaction between the airstream and the bladeless bodies, which is shown in Figure 3. Specific boundary conditions were set up in the computational simulation as shown in the same figure. The two bladeless bodies and the air flow are aligned in the same direction to the airstream in- and outflow indicated with two arrows, while symmetry regions were defined on the extreme walls of the domain, which eases the convergence of the solution. The friction between the wall and airstream was a key factor that allowed us to analyze the VIV on the upstream bladeless turbine and the subsequent interaction of the wake with the downstream bladeless turbine, taking into account the no-slip condition with the bottom wall. The flow inlet was defined as a velocity boundary condition, defined by the *Re* number. For one bladeless model, the mesh was similar. The mesh size was six bladeless heights, *h*, in length, two heights tall, and four heights wide.

Boundary conditions.	
Section	**Definition**
A	Inlet, velocity
B	Outlet, zero-pressure
C	Symmetry
D	Wall
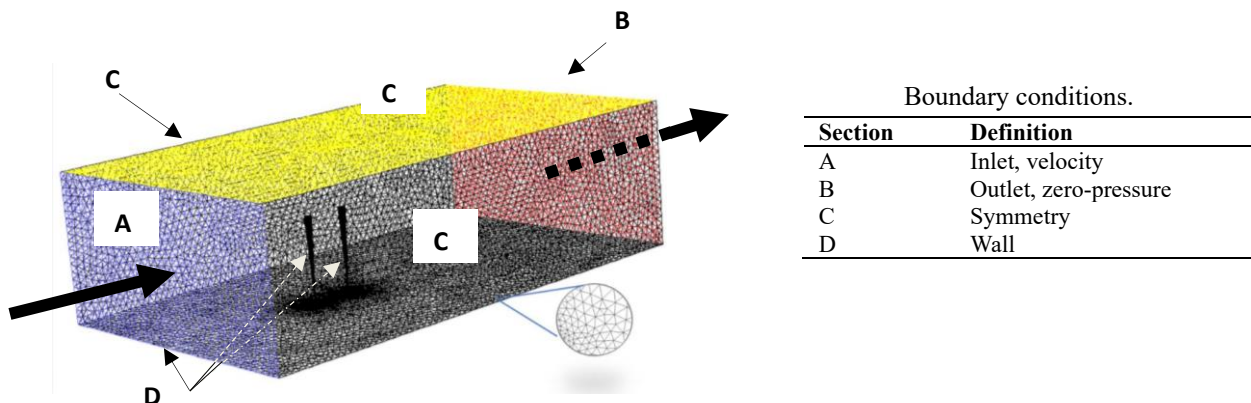
Figure 3. Computational mesh with non-structured elements used to simulate bladeless vortex shedding.

2.2.1. Mesh convergence

Table 1. Number of elements per mesh, and velocity results for the independence test.

Mesh	Single Conical Cylinder model		Distance between two conical cylinders					
			0.25h		0. 5h		0.75h	
	Cells x10^6	Velocity m/s	Cells x10^6	Velocity m/s	Cells x10^6	Velocity m/s	Cells x10^6	Velocity m/s
1	2.4	2.0210	3.8	1.9881	4.4	1.9556	1.4	2.2710
2	3.7	1.9158	4.5	1.8949	6.2	1.9245	3.1	2.1792
3	4.1	1.8985	5.4	1.9076	7.8	1.9249	4.5	1.8851
4	5.5	1.8986	7.8	1.9071	9.4	1.9240	6.2	1.8978

A refining of the mesh process included a gradual increase in the number of cells, to test for mesh convergence. The mesh convergence ended when a difference of results between the last two meshes was small enough to consider that the calculation did not depend on the number of cells. Monitors of velocity located near the bladeless models indicated this convergence. The results are shown in Table 1.

The process indicated how much the resulted velocity differentiated from a result obtained with a mesh with a smaller number of cells, as shown in Table 1, until it reached an error smaller than 1%. In summary, mesh number 4 was enough for conducting the CFD simulations, for cases of one and two conical cylinders.

2.2.2. Turbulence modeling

A 2-D CFD simulation for fluid-structure interaction solved the conservation equations of mass and momentum as a function of time [52]. The goal was to conduct a benchmark to decide which turbulence model better reproduced resonance conditions on the structure, which was detected by a wake of vortex shedding, as observed in Figure 4. The information to find was at what velocity it occurred. Vortex shedding may occur in the wake for a range of fluid velocity past a body, depending on the natural frequency f of the body, which was found through modal analysis conducted by FEM. The magnitude found was $f = 5.36$ Hz [53]. This result served as a guide to calibrate the simulation assuming as a key control the resonance velocity, at the natural frequency of the structure.

The results are shown in Table 2 for a set of velocity conditions. While all velocity conditions tabulated produced vortex shedding, only one is near to the velocity of resonance, which was found to be $U = 1.5\ m\ s^{-1}$. As observed in Table 2, all models approximate to the natural frequency of the bladeless generator for the condition $U = 1.5\ m\ s^{-1}$, with an error smaller than 3%, except Spallart. In addition, it is notorious that model k-ε standard predicts the frequency of the vortex with the smallest error, 1.31%, while models k-ε realizable and k-ω predict it with an error of 2.24%. Finally, the k-ε SST model had an error of 2.43%.

Table 2. Benchmark of turbulence models for a range velocity based on the natural frequency of the bladeless body.

Condition	Vortex shedding frequency Hz					
	Model tested for turbulence					
U ms^{-1}	Laminar	Spallart	k-ε standard	k-ε realizable	k-ω	k-ε SST
0.1	0.48	0.33	0.33	0.33	0.33	0.39
0.5	1.99	1.74	1.99	1.99	1.99	1.74
1	3.98	3.49	3.99	3.99	3.99	3.49
1.5	5.47	4.98	5.43	5.48	5.48	5.23
2	6.41	6.48	7.48	7.48	7.48	6.98
2.5	7.58	7.98	9.47	9.47	9.47	8.72

To finish the calibration of turbulence modeling, the analysis turned to verify which model best reproduced the Strouhal number, $St,$ defined as:

$$St = \frac{fd}{U} \tag{10}$$

where f represents a frequency for the detachment of the vortex, d is the diameter, and U is the upstream flow velocity. The reference value for this parameter is $St = 0.2$ [16,53–54], which, as

discussed above, is often related to the Re number:

$$Re = \frac{UL}{v} \tag{11}$$

where L is a characteristic length, the diameter, and v is the kinematic viscosity of the fluid. The results are in Table 3, including the solutions with four models for turbulence and a Re number for the velocity of resonance from Table 2. As observed, two models predict the St number with approximate accuracy, k-ε realizable and k-ω. This will be discussed below.
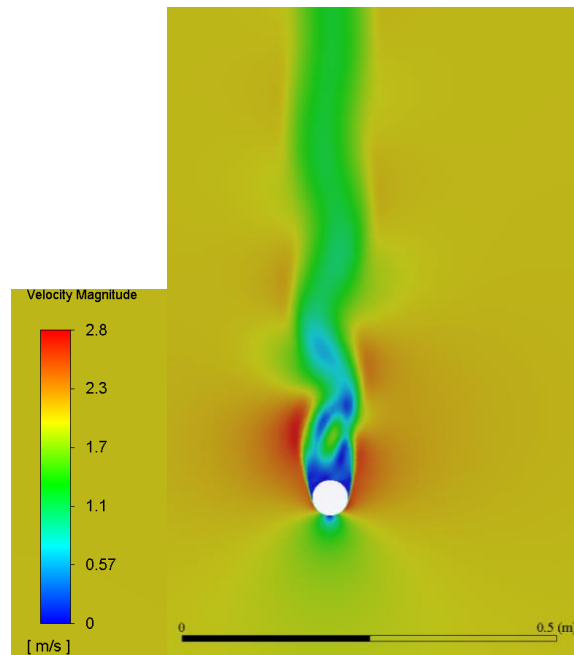

Figure 4. A 2-D computational simulation of vortex shedding.

Table 3. Comparison of turbulence models for the prediction of St for a velocity of resonance.

				Strouhal number		
Condition				Models tested for turbulence		
U ms^{-1}	Re x10^3	Re log	k-ε standard	k-ε realizable	k-ω	k-ε SST
1.5	4.88	3.7	0.172	0.173	0.173	0.165

2.3. *Validation of the numerical approach by comparison with experimental data*

The validation of the numerical approach presented above proceeded first by a comparison with the St number reported as $St = 0.2$ [20,54]. A whole set of predictions is shown in Figure 5, where the St number is plotted against the Re number. The plot indicates that the models k-ε realizable and k-ω follow the experimental results from the literature [54]. The results from these two models differ from the experimental data by only 3.6%, which is considered acceptable for subsequent computations. However, with a criterion based on minimizing the computational effort, the k-ε realizable model solution is preferred since it gets faster convergence compared to k-ω. Therefore, the results given in the next section refer only to the k-ε realizable model.
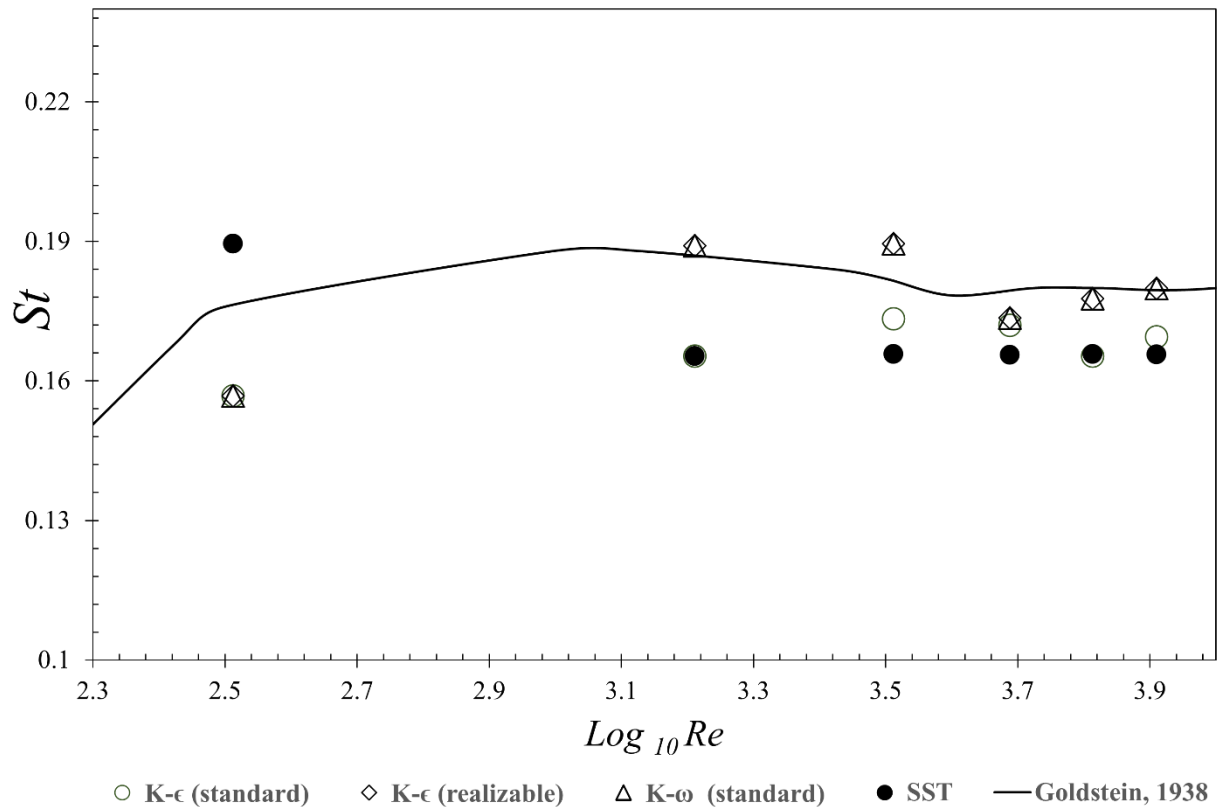
Figure 5. A comparison of 2-D modeling for the Strouhal number as a function of the Reynolds number for one cylinder past the fluid.

Subsequently, the numerical approach was validated against results from experimental wind tunnel modeling of a bladeless generator conducted by the authors, where details are being reported separately. The experiment was planned following reported work in the literature [54], adapted to an existing wind tunnel. For this reason, the experimental bladeless generator is a 1:2 scale model from the reported one [50]. The comparison of numerical to experimental results corresponds to a *Re* number for the middle diameter. All settings of both models are shown in Table 4. As observed, the conditions for fluid flow are the same, meaning that a value for displacement of oscillation is experimentally smaller than the numerical one because of the scale effect.

Table 4. Main conditions of wind tunnel experimental and numerical modeling.

Condition		Operating oscillation (Resonance)		Geometry				Materials	
U ms^{-1}	Re x10^3	Amplitude mm	Velocity mm s^{-1}	d_{min} mm	d_{max} mm	h mm	pivot	Conical cylinder	
Experimental model									
5.14	4.82	8.83	89.7	5	23.75	268.5	Carbon fiber	Polylactic acid	
Numerical model									
1.5	4.88	16.8	-	10	47.5	578.5	Carbon fiber	Polylactic acid	

In both models, since the material properties were identical, the reduced mass was 139 in the numerical model and 278 in the experimental model. Since the numerical approach was for a not-flexible bladeless generator, the amplitude of oscillation was calculated with harmonic analysis, based on FEM. This methodology did not allow us to numerically obtain a resonance velocity of oscillation as observed in column four of Table 4. So, this parameter could not be compared. Despite this limitation, the accuracy of the numerical solution led to a small discrepancy of 5.1% between the numerical and experimental results for the amplitude of the operating oscillation. Therefore, based on this result and the validation against another source [54], the numerical approach was considered acceptable.

3. Results and Discussion

3.1. 2-D simulation of tandem cylinder distribution

| a | b | c |
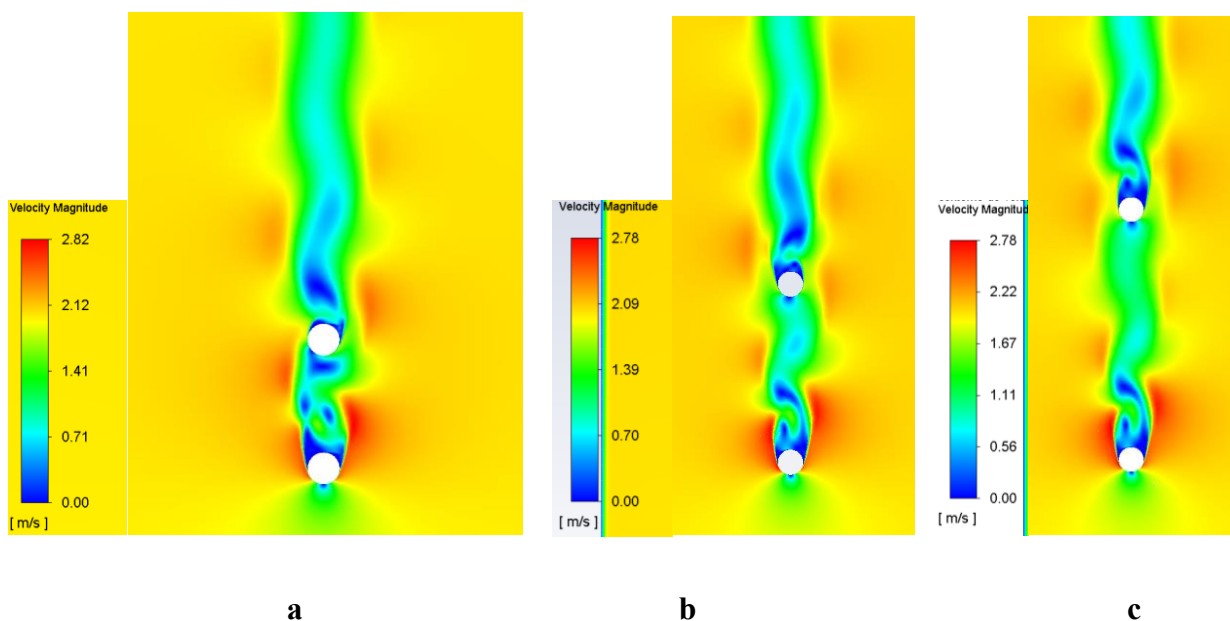
Figure 6. A 2-D computational simulation of vortex shedding for tandem bladeless generators for $Re = 4.88 \times 10^3$; a) $\ell = 0.25h$; b) $\ell = 0.5h$; c) $\ell = 0.75h$.

Next, we will glance at the worth of the time dependent solution of past flow over two 2-D bladeless generators in tandem distribution. The results of several monitors placed strategically around the cylinders show the effects. The vortex shedding presents strong discrepancy between the first and second cylinders due to the distance of separation ℓ. The results are shown in the form of colored contours of velocity in Figure 6 for the three distances of separation for the tandem cylinders. Focusing the attention on the wake of the first cylinder, we see that the wake is defined by a region of separation of the boundary layer, marked with zero velocity, and it looks similar for three distances as shown in Figures 6a–c. However, an effect on the wake in front of the second cylinder is evident, especially for the shortest distance $\ell = 0.25h$ in Figure 6a, because a modified pressure field affects and deforms the second vortex. This effect makes flow distribution different on the second cylinder, preventing the development of vortex shedding, which is responsible for the oscillatory vibration, especially affecting the amplitude of this oscillation. Instead, a second vortex pair is in course with a distance separation

of $\ell = 0.5h$ in Figure 6b, with little effect on the flow distribution for the second cylinder. Finally, the distance of separation $\ell = 0.75h$ represents a safe configuration for the development of the vortex and the effect of vortex shedding for the second cylinder seems minimal.
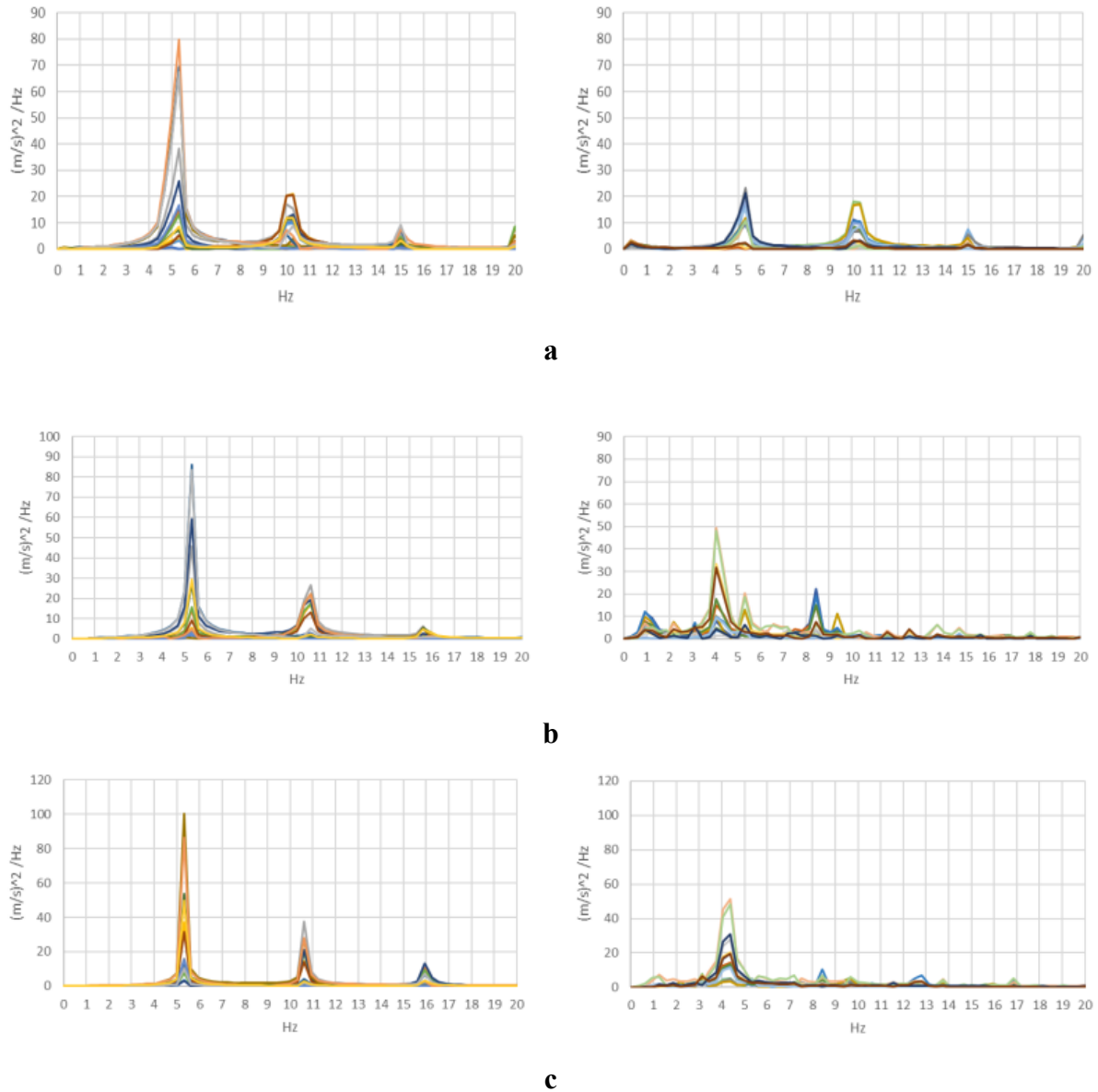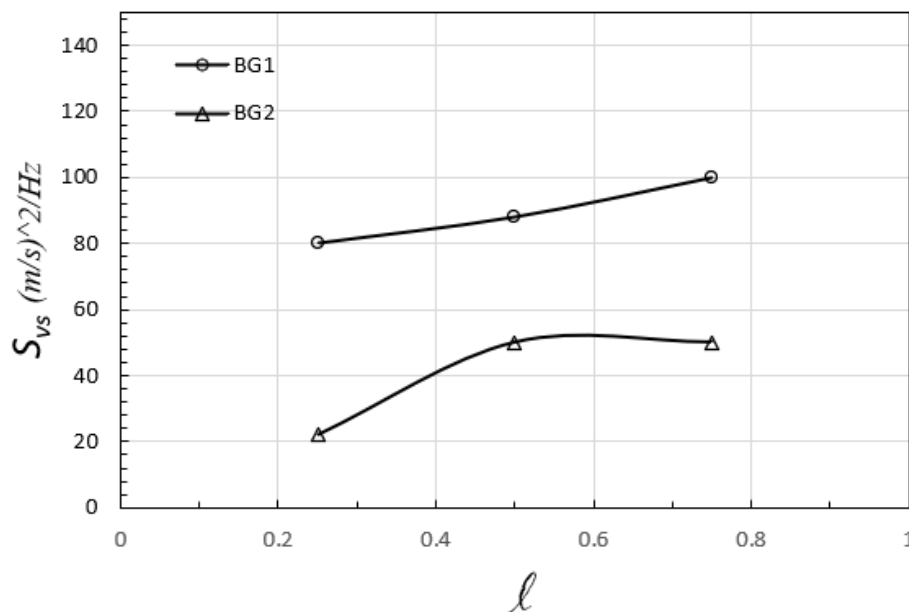

Figure 7. Spectrum of vortex shedding frequency from 2-D computational simulation for the first cylinder on the left, and for the second cylinder on the right; a) $\ell = 0.25\ h$; b) $\ell = 0.5\ h$; c) $\ell = 0.75\ h$.

The results in Figures 6a–c are congruent with the frequency of detachment, which is part of the analysis for the first and second cylinders, as presented in Table 5. This table shows that the medium distance of separation between the cylinders makes a strong effect on vortex shedding frequency for the second cylinder. The second cylinder presents a reduction of 25.3%, compared to the frequency of the first cylinder. It is assumed that the energy from this reduction distributes over other frequencies, since the spectrum of vortex shedding frequencies shows many more frequencies for the second

cylinder than for the first cylinder, as observed in Figures 7a–c. In agreement with Table 4, the results for the shortest distance of separation, Figure 7a shows unaltered frequencies for the middle distance $\ell = 0.5 \ h$ of separation, compared to the first cylinder on the left, except for reduced amplitude. The reduction for amplitude on the spectrum of vortex shedding frequency may be considered as a second effect of the distance of separation between the first and second cylinders. The distance from the first one that most affects the second cylinder in this respect is $0.25h$. In summary, while the frequency of vortex shedding remains constant for the first BG1, for all separation distances l (see Table 5), its amplitude of spectrum increases little, compared to the effects on the second cylinder BG2, as observed in Figure 8. This figure shows a plot of spectrum against distance of separation, where a strong effect of reduction on the second tandem cylinder is observed.

Table 5. Numerical simulation results for tandem bladeless generators (BG).

| Distance of separation ℓ	Re x10³	Detachment frequency BG1 Hz	Detachment frequency BG2 Hz
0.25 h	4.88	5.3125	5.3125
0. 5 h	4.88	5.3125	4.0625
0.75 h	4.88	5.3125	4.375

Figure 8. Amplitude of spectrum of vortex shedding for each cylinder BG1 and BG2, as a function of separation distance ℓ.

The amplitude of oscillation S_{vs} is a parameter that deserves special attention together with the frequency of oscillation in energy harvesting, since it affects the efficiency of the harvester. Although for BG1, there is no difference of amplitude between the separation distances $0.5h$ and $0.75h$, a reduction of 54% results for the amplitude for BG2 compared to the first one, as observed in Figure 8. From this result on, it is clear that the efficiency of BG2 reduces drastically.

3.2. 3-D simulation of tandem cylinder distribution

The 3-D numerical simulation is conducted using grid 4 of Table 1, shown in Figure 3. The results are presented in streamlines to represent and display the wake displacement through side views, as observed in Figures 9a–c. The closer the tandem cylinders, the more the effect of the first has on the second. In addition, the conical shape of the cylinders renders uneven distribution of the wake, especially for separation distances $0.25h$ and $0.5h$. Instead, Figure 9c shows that a larger separation distance like $0.75h$ has little effect on the wake from each other. By comparison, a single cylinder is presented in Figure 9d. The wake is observed to present the largest displacement in the stream direction of fluid flow in a height position $h = 75\%$, which is in agreement only with the result for a separation distance $\ell = 0.5h$, since it gives the smaller effect of wakes as discussed above. However, by analyzing the wake for separation distance $\ell = 0.75h$, a totally different result is observed. Although compressibility of air is small, the effect at this separation distance affects them both upstream and downstream.
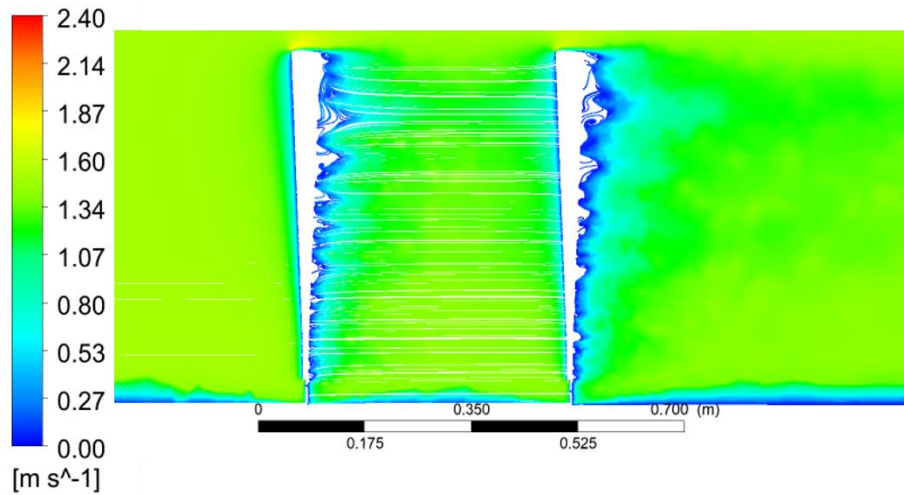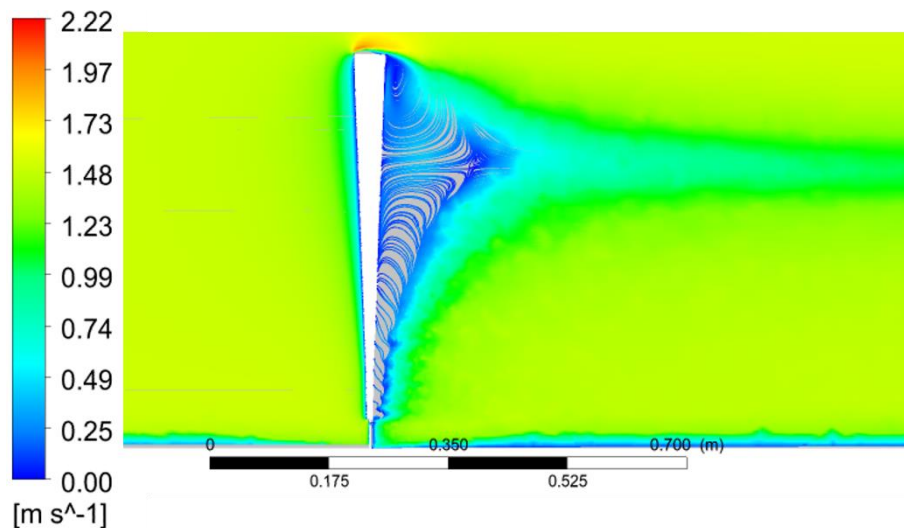

a

b
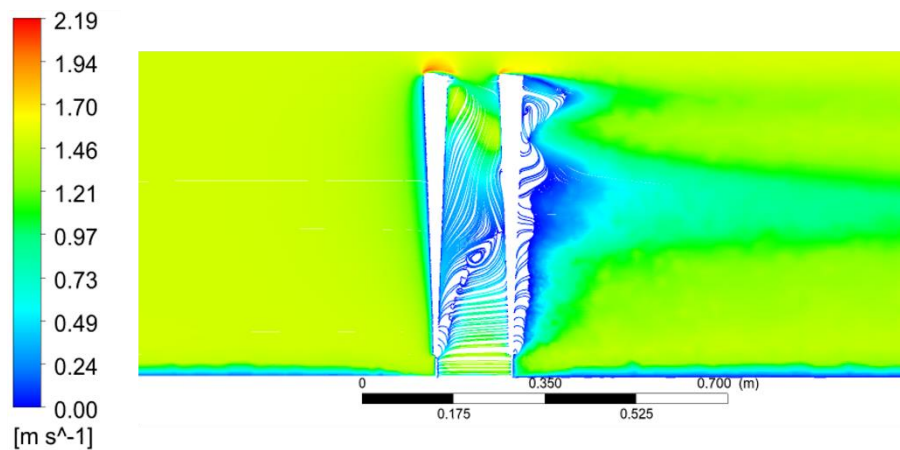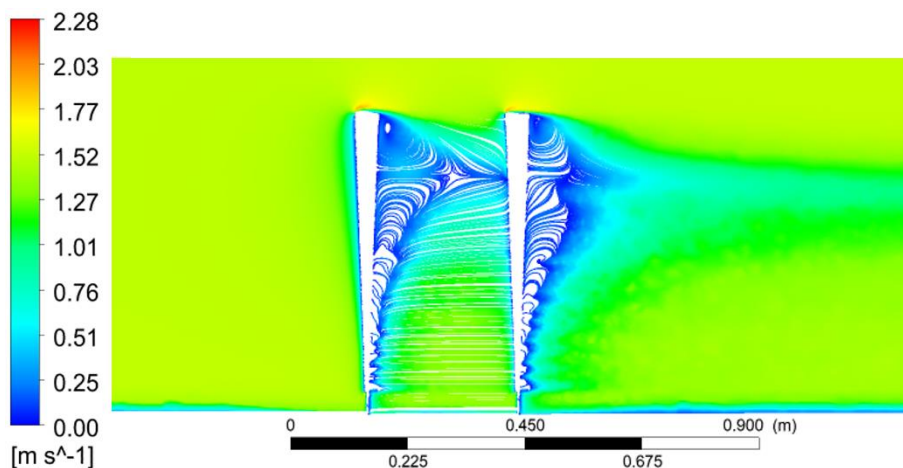
c


d

Figure 9. Streamlines for 3-D numerical solution vortex shedding for $Re = 4.88 \times 10^3$, as a function of the separation distance; a) $\ell = 0.25h$; b) $\ell = 0.5h$; c) $\ell = 0.75h$; d) single bladeless generator.

After analyzing the results in a 3-D solution, the pressure field was defined for each cylinder and for three distances of separation. The pressure field was used as a boundary condition in a FEM solution for harmonics analysis. The results of this modeling allowed us to determine the amplitude of oscillation displacement, which is shown in Figure 10 for each cylinder.

As expected, the oscillation amplitude for the downstream tandem cylinder becomes affected by the first cylinder. The difference with the upstream tandem cylinder is up to 58.3% smaller for a short separation distance $0.25h$, while the difference reduces to 22% for the larger distance $0.75h$. Instead, for the middle separation distance $0.5h$, the difference of amplitude reduces to 33%.
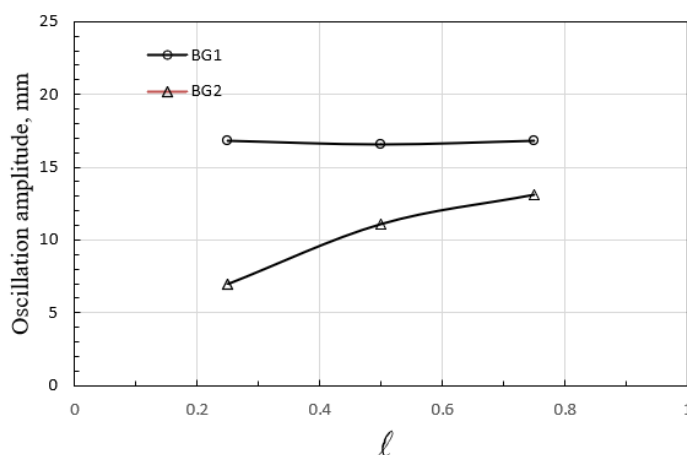
Figure 10. Effect on oscillation displacement from the first to the second bladeless generator for $Re = 4.88 \times 10^3$, as a function of separation distance.

4. Conclusions

The paper presents results from numerical solutions of fluid flow past a bladeless turbine and its effects on a second tandem bladeless turbine. The work focused on oscillating cylinders of varying diameter, with slenderness ratio, $H = 0.045$. The goal was to define the best separation distance between them, judged by the maximum amplitude of vibration and the frequency of oscillation for the downstream one, which are affected by the wake of vortex shedding. As a benchmark, looking at the solutions obtained with four different turbulence models, the k-ε realizable model was the best option for this case. A flowchart showing the route for numerical predictions was defined using combined CFD and FEM. The main effects are observed in the bladeless turbine placed downstream, through a reduction of oscillation displacement, and of the frequency of oscillation. The results indicate that as the separation distance between both turbines decreases, the difference in displacement amplitude increases, with the upstream turbine exhibiting the maximum amplitude. Therefore, from the three separations studied, it was observed that $\ell = 0.75h$ causes the least difference in displacement amplitude between the upstream and downstream turbines. This is because the closer the bodies are, the greater the disturbance the upstream body generates on the downstream body, subjecting the second body to excitations that do not necessarily correspond to its natural frequency. Future directions for the research are: evaluating the vibration modes of single and tandem bladeless turbines and investigating how the vibration modes relate with the power output for both resonance and near resonance conditions.

Use of AI tools declaration

The authors declare they have not used Artificial Intelligence (AI) tools in the creation of this article.

Acknowledgments

Author contributions

All authors contributed to the study conception and design. The material preparation, data collection and analysis performed by [D.M. Graciano, F.Z. Sierra-Espinosa and J.C. García]. A first draft written by [D.M. Graciano and F.Z. Sierra-Espinosa] and author [J.C. García] contributed with signal processing. All authors read and approved the final manuscript.

Conflict of interest

The authors have no relevant financial or non-financial interests to disclose.

References

1. Nair AR, Jaiswal V, McGinty TD (2018) Riser Vortex-Induced Vibrations. *Encyclopedia Marit Offshore Eng* 2017: 1–12. https://doi.org/10.1002/9781118476406.emoe492
2. Bhatt R, Alam MM (2018) Vibrations of a square cylinder submerged in a wake. *J Fluid Mech* 853: 301–332. https://doi.org/10.1017/jfm.2018.573
3. Huang Z, Ong MC, Larsen CM (2019) Wake structures and vortex-induced forces of a controlled in-line vibrating circular cylinder. *Ocean Eng* 189. https://doi.org/10.1016/j.oceaneng.2019.106319
4. Janocha MJ, Ong MC, Nystrøm PR, et al. (2021) Flow around two elastically-mounted cylinders with different diameters in tandem and staggered configurations in the subcritical Reynolds number regime. *Mar Struct* 76. https://doi.org/10.1016/j.marstruc.2020.102893
5. Li JH, Wang BF, Qiu X, et al. (2024) Vortex dynamics and boundary layer transition in flow around a rectangular cylinder with different aspect ratios at medium Reynolds number. *J Fluid Mech* 982: A5. https://doi.org/ 10.1017/jfm.2024.87
6. Muyshondt R, Nguyen T, Hassan YA, et al. (2021) Experimental measurements of the wake of a sphere at subcritical reynolds numbers. *J Fluid Eng-T Asme* 143: 061301. https://doi.org/10.1115/1.4049936
7. Rahman H, Khan IA, Abbasi WS, et al. (2024) Aerodynamic characteristics and wake formation behind a pair of side-by-side rectangular cylinders using the lattice Boltzmann method. *Ocean Eng* 303: 117813. https://doi.org/10.1016/j.oceaneng.2024.117813
8. Chen W, Ji C, Alam Md M, et al. (2022) Three-dimensional flow past two stationary side-by-side circular cylinders. *Ocean Eng* 244: 110379. https://doi.org/10.1016/j.oceaneng.2019.106319
9. Kumar A, Das S P, Tiwari S (2024) Wall effect on the wake characteristics of a transversely rotating sphere. *Phys Fluids* 36. https://doi.org/10.1063/5.0180332
10. Liu H, Li H, Wang H, et al. (2024) Effects of a detached splitter on the vortex-induced vibration of a 5: 1 rectangular cylinder. *Phys Fluids* 36. https://doi.org/10.1063/5.0183812
11. Wang W, Duan P (2024) Vortex-induced vibration response of the cylinder inspired by Terebridae. *Mar Structures* 94: 103575. https://doi.org/10.1016/j.marstruc.2024.103575
12. Ashouri A, Izadpanah E, Hekmat MH, et al. (2021) Numerical investigation on two-degree-of-freedom vortex-induced vibration of a circular cylinder in power-law fluids. *J Nonnewton Fluid Mech* 292. https://doi.org/10.1016/j.jnnfm.2021.104535
13. Achenbach E (1974) Vortex Shedding from Spheres. *J Fluid Mech* 62. https://doi.org/10.1017/S0022112074000644

14. Gerrard JH (1966) The mechanics of the formation region of vortices behind bluff bodies. *J Fluid Mech* 25: 401–413. https://doi.org/ 10.1017/S0022112066001721

15. Jiang H, Cheng L (2017) Strouhal-Reynolds number relationship for flow past a circular cylinder. *J Fluid Mech* 832: 170–188. https://doi.org/ 10.1017/jfm.2017.685

16. Liu Y, Liu J, Gao FP (2023) Strouhal number for boundary shear flow past a circular cylinder in the subcritical flow regime. *Ocean Eng* 269: 113574. https://doi.org/10.1016/j.oceaneng.2022.113574

17. Derakhshandeh JF (2024) Wake-induced vibration of an elastic plate submerged in the wake of tandem circular cylinders. *Phys Fluids* 36: 033623. https://doi.org/10.1063/5.0199501

18. Ramalingam S, Huang RF, Hsu CM (2023) Effect of crossflow oscillation Strouhal number on circular cylinder wake. *Phys Fluids* 35: 95118. https://doi.org/10.1063/5.0168618

19. Wang Y, Lou M, Liang W, et al. (2024) Dynamic evolution of Strouhal number in flexible pipes coupling rotation. *Int J Mech Sci* 263: 108783. https://doi.org/10.1016/j.ijmecsci.2023.108783

20. el Sheshtawy H, Toedter S, el Moctar O, et al. (2021) Experimentally investigated vortex-induced vibration of a high aspect ratio and small mass ratio circular cylinder oscillating in low reduced velocity flows. *Ocean Eng* 238. https://doi.org/10.1016/j.oceaneng.2021.109735

21. Ponta FL, Aref H (2004) Strouhal-Reynolds Number Relationship for Vortex Streets. *Phys Rev Lett* 93: 084501. https://doi.org/10.1103/PhysRevLett.93.084501

22. Williamson CHK, Brown GL (1998) A series in L/ √ Re to represent the Strouhal‐Reynolds number relationship of the cylinder wake. *J Fluids Struct* 12: 1073–1085. https://doi.org/10.1006/jfls.1998.0184

23. Williamson CHK (1996) Vortex Dynamics in the Cylinder Wake. *Annu Rev Fluid Mech* 28: 477–539. https://doi.org/10.1146/annurev.fl.28.010196.002401

24. Fey U, König M, Eckelmann H (1998) A new Strouhal–Reynolds-number relationship for the circular cylinder in the range 47&lt;Re&lt;2×105. *Phys Fluids* 10: 1547–1549. https://doi.org/10.1063/1.869675

25. Derakhshandeh JF, Alam MM (2019) A review of bluff body wakes. *Ocean Eng* 182: 475–488. https://doi.org/10.1016/j.oceaneng.2019.04.093

26. Bernitsas MM, Raghavan K, Ben-Simon Y, et al. (2006) VIVACE (Vortex Induced Vibration Aquatic Clean Energy): A New Concept in Generation of Clean and Renewable Energy From Fluid Flow. in *Volume 2: Ocean Engineering and Polar and Arctic Sciences and Technology*, 619–637. https://doi.org/10.1115/OMAE2006-92645

27. Raghavan K, Bernitsas MM (2011) Experimental investigation of Reynolds number effect on vortex induced vibration of rigid circular cylinder on elastic supports. *Ocean Eng* 38: 719–731. https://doi.org/10.1016/j.oceaneng.2010.09.003

28. Villarreal Yañez DJ (2018) Vortex resonance wind turbine. Available from: https://www.researchgate.net/profile/David-J-Yanez/publication/.

29. Chizfahm A, Yazdi EA, Eghtesad M (2018) Dynamic modeling of vortex induced vibration wind turbines. *Renew Energ* 121: 632–643. https://doi.org/10.1016/j.renene.2018.01.038

30. González-González E, Yáñez DJ, Del Pozo S, et al. (2024) Optimizing Bladeless Wind Turbines: Morphological Analysis and Lock-In Range Variations. *Appl Sci* 14: 2815. https://doi.org/10.3390/app14072815

31. Sun H, Ma C, Kim ES, et al. (2017) Hydrokinetic energy conversion by two rough tandem-cylinders in flow induced motions: Effect of spacing and stiffness. *Renew Energ* 107: 61–80. https://doi.org/ 10.1016/j.renene.2017.01.043

32. Lam K, Fang X (1995) The Effect of Interference of Four Equispaced Cylinders in Cross Flow on Pressure and Force Coefficients. *J Fluids Struct* 9: 195–214. https://doi.org/10.1006/jfls.1995.1010

33. Lam K, Li JY, So RMC (2003) Force coefficients and Strouhal numbers of four cylinders in cross flow. *J Fluids Struct* 18: 305–324. https://doi.org/10.1016/j.jfluidstructs.2003.07.008

34. Zou L, Lin Y, Lam K (2008) Large-Eddy Simulation of Flow Around Cylinder Arrays at a Subcritical Reynolds Number. *J Hydrodyn* 20: 403–413. https://doi.org/10.1016/j.jfluidstructs.2003.07.008

35. Kahil Y, Benhamadouche S, Berrouk AS, et al. (2019) Simulation of subcritical-Reynolds-number flow around four cylinders in square arrangement configuration using LES. *Eur J Mech-B/Fluids* 74: 111–122. https://doi.org/ 10.1016/j.euromechflu.2018.11.008

36. Pouryoussefi SG, Mirzaei M, Pouryoussefi SMH (2011) Force coefficients and Strouhal numbers of three circular cylinders subjected to a cross-flow. *Arch Appl Mech* 81: 1725–1741. https://doi.org/10.1007/s00419-011-0514-3

37. Kim S, Alam MM, Sakamoto H, et al. (2009) Flow-induced vibrations of two circular cylinders in tandem arrangement. Part 1: Characteristics of vibration. *J Wind Eng Ind Aerod* 97: 304–311. https://doi.org/10.1016/j.jweia.2009.07.004

38. Xu W, Ji C, Sun H, et al. (2019) Flow-induced vibration of two elastically mounted tandem cylinders in cross-flow at subcritical Reynolds numbers. *Ocean Eng* 173: 375–387. https://doi.org/10.1016/j.oceaneng.2019.01.016

39. Assi GRS, Bearman PW, Carmo BS, et al. (2013) The role of wake stiffness on the wake-induced vibration of the downstream cylinder of a tandem pair. *J Fluid Mech* 718: 210–245. https://doi.org/10.1017/jfm.2012.606

40. Kim ES, Bernitsas MM (2016) Performance prediction of horizontal hydrokinetic energy converter using multiple-cylinder synergy in flow induced motion. *Appl Energ* 170: 92–100. https://doi.org/10.1016/j.apenergy.2016.02.116

41. Kim ES, Bernitsas MM, Kumar RA (2011) Multi-Cylinder Flow-Induced Motions: Enhancement by Passive Turbulence Control at 28,000<Re<120,000. in *Volume 7: CFD and VIV; Offshore Geotechnics,* 249–260. https://doi.org/10.1115/OMAE2011-49405

42. Ding L, Bernitsas MM, Kim ES (2013) 2-D URANS vs. experiments of flow induced motions of two circular cylinders in tandem with passive turbulence control for 30,000<Re<105,000. *Ocean Eng* 72: 429–440. https://doi.org/10.1016/j.oceaneng.2013.06.005

43. Vandiver KJ, Cheng Y, Jaiswal V, et al. (2009) An experimental evaluation of vortex-induced vibration of a riser bundle with gaps. *Proc of the ASME 28th Int Conf on Ocean, Offshore and Arctic Engineering*, Honolulu. https://doi.org/10.1115/OMAE2009-79757

44. Haider BA, Sohn CH (2018) Effect of spacing on a pair of naturally oscillating circular cylinders in tandem arrangements employing IB-LB methods: Crossflow-induced vibrations. *Int J Mech Sci* 142–143, 74–85. https://doi.org/10.1016/j.ijmecsci.2018.04.032

45. Song R, Shan X, Lv F, et al. (2015) A study of vortex-induced energy harvesting from water using PZT piezoelectric cantilever with cylindrical extension. *Ceram Int* 41: S768–S773. https://doi.org/10.1016/j.ceramint.2015.03.262

46. Lai Z, Wang S, Zhu L, et al. (2021) A hybrid piezo-dielectric wind energy harvester for high-performance vortex-induced vibration energy harvesting. *Mech Syst Signal Process* 150: 107212. https://doi.org/10.1016/j.ymssp.2020.107212

47. Yuan W, Sun H, Li H, et al. (2020) Flow-induced oscillation patterns for two tandem cylinders with turbulence stimulation and variable stiffness and damping. *Ocean Eng* 218: 108237. https://doi.org/10.1016/j.oceaneng.2020.108237

48. Williamson CHK, Govardhan R (2004) VORTEX-INDUCED VIBRATIONS. *Annu Rev Fluid Mech* 36: 413–455. https://doi.org/10.1146/annurev.fluid.36.050802.122128

49. Govardhan R, Williamson CHK (2000) Modes of vortex formation and frequency response of a freely vibrating cylinder. *J Fluid Mech* 420: 85–130. https://doi.org/10.1017/S0022112000001233

50. Cajas JC, Pastrana D, Rodríguez I, et al. (2021) Vortex induced vibrations of a pivoted finite height cylinder at low Reynolds number. *Phys Fluid* 33. http://doi.org/10.1063/5.0051689

51. Kara MC, Jaiswal V, Sharma PP, et al. (2018) Numerical Modeling of High Length-to-Diameter Ratio Riser Subjected to VIV. Paper presented at the Offshore Technology Conference, Houston, Texas, USA. https://doi.org/10.4043/28635-MS

52. Ferziger J, Peric M (1996) Computational methods for fluid dynamics, Springer-Verlag, Berlin Heidelberg. https://doi.org/10.1007/978-3-319-99693-6

53. Graciano DM (2020) Determination of the wake vortex effect on the oscillation of a group of wind generators by vorticity, Master Thesis, State of Morelos University, Center for Research in Engineering and Applied Sciences, UAEM, Cuernavaca, Mexico.

54. Goldstein S (1938) *Modern developments in fluid dynamics; an account of theory and experiment relating to boundary layers, turbulent motion and wakes*. Oxford: Cambridge University Press.